Kovove Mater. 63 2025 233–249
DOI: 10.31577/km.2025.4.233

The microstructure and flow behavior of a hot-deformed titanium alloy

Yu-Qiang Jiang[1,2], Min-Bo Wang[1], Chong-Rui Wu[1], Yi-Fei Zhang[1], Jing-Jing Han[1], Dong Wu[1], Zhi-Fang Huang[2]*

[1]*School of Materials Science and Engineering, East China Jiaotong University, Nanchang 330013, P. R. China*
[2]*School of Chemistry and Food Science, Nanchang Normal University, Nanchang 330032, P. R. China*

Received 6 May 2025, received in revised form 22 October 2025, accepted 29 October 2025

Abstract

Titanium alloys are ideal materials for load-bearing components, and hot forming is the primary method for manufacturing these parts. In this work, the hot deformation behavior and microstructure of an anti-damage titanium alloy are studied, and a phenomenological constitutive model is established. The results show that hot deformation has little effect on the shape of the equiaxial α phase, and the α phase retains its equiaxial morphology. The size and fraction of the α phase vary with the hot-deformation parameters. The dynamic phase transformation, Ostwald ripening, and spheroidization occur simultaneously during hot deformation. An Arrhenius constitutive equation is established with a correlation coefficient of 0.9848, and the model can be utilized to predict the flow behavior of the studied titanium alloys at high-temperature deformation.

K e y w o r d s: microstructure, hot deformation, titanium alloy, constitutive modeling

1. Introduction

Among steel and lightweight alloys, titanium alloys are crucial in load-bearing parts owing to their significant damage tolerance and high specific strength [1–8]. Thermomechanical processing (TMP) is the preferred method for manufacturing titanium alloy parts to achieve excellent mechanical properties, such as strength, fatigue life, and fracture toughness [9–14]. The relationships among the microstructure, flow behavior, and TMP-forming parameters must be clarified to optimize the comprehensive mechanical properties of titanium alloy components.

Due to the multiscale microstructural characteristics, the microstructural development of titanium alloys is complicated. According to the TMP parameters, work hardening (WH), dynamic recovery (DRV), static/dynamic/meta-recrystallization (SDRX, MDRX, DRX), dynamic phase transformation (DPT), and texture evolution (TE) may occur to varying degrees [15–19]. Generally, in alloys deformed in the single-phase zone, WH and DRV are the main deformation mechanisms in the β phase, and DRX is rare. Jiang et al. [20] reported the DRX in a Ti-55511 alloy. Liu et al. [21] confirmed a novel refinement mechanism for ultra-large β grains. However, when titanium alloys are deformed in the $\alpha + \beta$ phase region, various mechanisms of α-phase evolution are observed, and the interaction between the α and β phases also significantly affects α-phase evolution. One of the eye-catching features is the spheroidization of the α phase, and the β-phase wedging and terminal migration are the main mechanisms of spheroidization [22, 23]. The DPT is another evolution mechanism. The microstructural evolution of the constituent phases in a titanium alloy is influenced by deformation parameters, the initial microstructure, and deformation modes [24]. Huang et al. [25] reviewed the microstructure of high-strength β titanium alloys in the hot deformation process. Zhang et al. [26] prepared a heterogeneous structure with lamellar microstructures and ultrafine grains using a four-step multidirectional forging and annealing process. Su et al. [27] investigated the DPT at 1263 K. Jiang et al. [28] addressed kinking in TA15 titanium

*Corresponding author: tel.: +86-15874284547, e-mail addresses: gugeyouling@163.com, huangzf0325@163.com

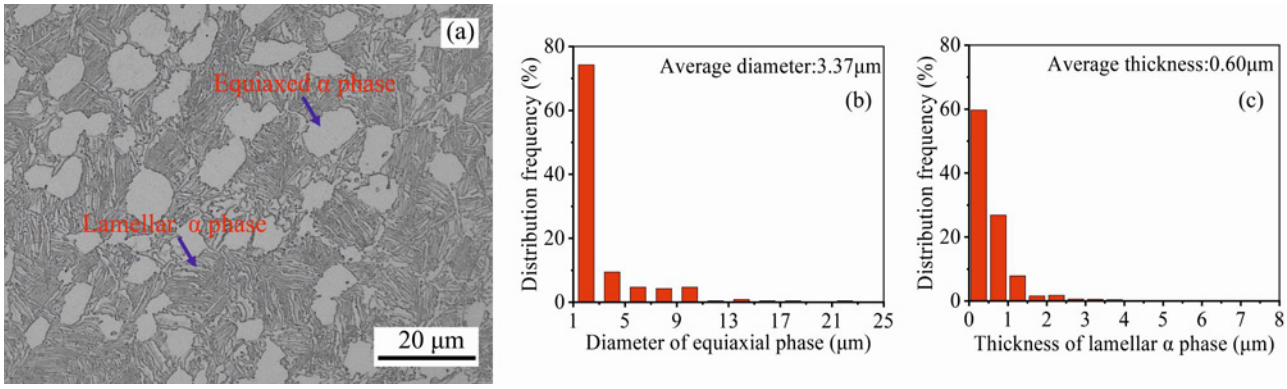

Fig. 1. Initial microstructure of the as-received alloy: (a) OM, (b) diameter distribution of equiaxed α phase, and (c) thickness distribution of lamellar α phase.

alloy and analyzed strain partitioning and intercolony interactions using a two-scale crystal plasticity model.

To predict the complicated deformation and microstructure in titanium alloys, numerous constitutive models have been developed [29, 30]. Yang et al. [31] developed a physically based constitutive model. Zhang et al. [32] proposed an elasto-viscoplastic constitutive model that incorporates dislocation density, WH, DRV, DRX, and JMAK-based DRX kinetics. In the two-phase titanium alloy, the constituent phases exhibit different deformation behaviors due to their HCP and FCC structures. Therefore, Buzolin et al. [33] proposed a mesoscale approach to describe the complex interactions among different populations of dislocation densities and predicted the flow stresses of both α and β phases using constitutive equations. Jha et al. [34] compared the flow softening of equiaxed and lamellar α phases in Ti-6Al-4V alloy, and the correlation between flow stress and the equiaxed and lamellar morphologies was observed. Wu et al. [35] reported the CDRX behavior of Ti-55511 using a cellular automata model, and integrated dislocation density, sub-grain nucleation, misorientation, grain boundary migration, and topology deformation models into the proposed cellular automata model. In recent years, the machine learning methods in constitutive modeling have become increasingly popular [36–38]. Wu et al. [39] predicted the high-temperature deformation behavior of a titanium alloy using a data-driven time-series deep learning approach. Hong et al. [40] predicted the flow stress in TC17 alloy using multiple prediction models. Using a machine learning and FEM simulation approach, Kim et al. [41] optimized the process parameters of a hot-forged Ti-6242 alloy.

Typically, the Ti-6Al-2Sn-2Zr-3Mo-1Cr-2Nb alloy (TC21 alloy) is successfully used in airframes due to its damage-tolerant characteristics. The mechanical properties of this alloy are especially sensitive to the microstructure and the TMP parameters. Wang et al. [42] reported that the micro-stress distribution depends on crystal orientation in this titanium alloy. Li et al. [43] investigated the hot deformation characteristics of a lamellar TC21 titanium alloy, and the globalization mechanism of the lamellar α phase involves the formation of a groove, localized shear deformation, and subgrain in α lamellae, which is followed by the penetration of β phase into α lamellae along the groove. Li et al. [44] optimized the quasi-β forging parameters, resulting in a trimodal microstructure in these titanium alloy forgings. In the damage-tolerant alloy, the α colony is a key microstructure correlated with the alloy's strength [45]. Thus, it is meaningful to systematically study the hot deformation and microstructure of a titanium alloy under different TMP conditions.

However, recent work is mainly focused on common commercial titanium alloys, and there are few related investigations of damage-tolerant titanium alloys. In this study, the high-temperature deformation behavior of the Ti-6Al-2Sn-2Zr-3Mo-1Cr-2Nb alloy was investigated using hot-compression testing, and the microstructural evolution of the alloy was characterized. A constitutive model of deformation was developed, and its accuracy was evaluated. The findings of this work can provide valuable insights for the development of TMP designs for the Ti alloys.

2. Materials and methods

A titanium alloy bar with the chemical constituents of 6.4Al-3.0Mo-2.1Zr-2.1Sn-1.9Nb-1.5Cr-Ti (Bal.) was used in this work, and the metallurgical measured β transition temperature is 1243 K. The original alloy is mainly made up of equiaxed and lamellar α phases, which is a typical bi-modal microstructure, as shown in Fig. 1a. The α phase with a length-width ratio less than 2.5 is regarded as the equiaxed α phase, while the length-width ratio larger than 2.5 is called the lamellar α phase. Figures 1b,c show the size distributions of the equiaxed and lamellar phases. According to optical micrographs (OM),

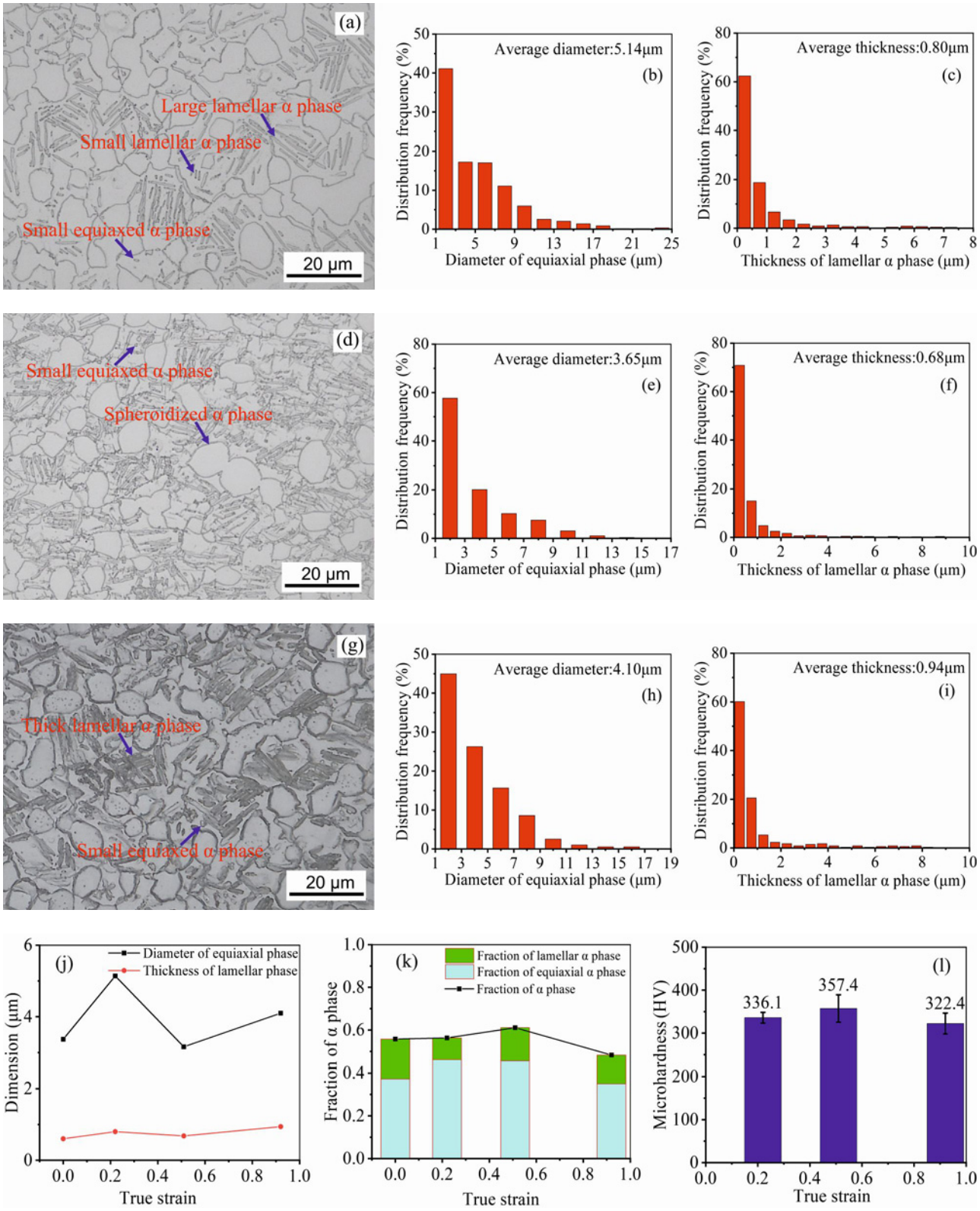

Fig. 2. The OM at 1173 K, 0.1 s^{-1} and true strains of: (a)–(c) 0.22, (d)–(f) 0.51, (g)–(i) 0.92, (j) dimension of α phase, (k) fraction of α phase, and (l) microhardness.

the α-phase fraction in the original titanium alloy bar is about 55.8 %. Among the α phase, the volume fraction of the equiaxed phases with an average diameter of 3.37 μm is 66.8 %, while the average thickness of lamellar α phases is 0.60 μm.

The ø 10 mm × 15 mm cylindrical samples were

used for the high-temperature compression experiments, and the Gleeble-3500 thermal simulator was used for the high-temperature compression experiments. Four deformation temperatures (1093, 1133, 1173, and 1213 K) and strain rates (0.001, 0.01, 0.1, and 1 s^{-1}) were adopted, and the engineering strains were 0.2, 0.4, and 0.6, i.e., the true strains were 0.22, 0.51, and 0.92, respectively. After the hot compression experiments, the microstructures were counted using *Image-Pro Plus 6.0*. The detailed experimental and characterization procedural details are reported in the prior publications of the authors [46, 47].

3. Microstructural evolution during the TMP process

3.1. Effect of strain

Figure 2 shows the microstructure of the studied alloy deformed at 1173 K and 0.1 s^{-1}, with different true strains. It can be found in Figs. 1–2, that the true strain has a significant influence on the microstructure of the studied alloy. The diameter of the equiaxed α phase, the thickness lamellar α phase, as well as the fraction of equiaxed and lamellar α phases are changed with the strains, as shown in Fig. 2. For the as-received alloy, the equiaxed and lamellar α phases are evenly dispersed in the β matrix in Fig. 1a. There are also some large bulk α phases in the β matrix, and the bulk α phase is not incomplete globalization. This is because the original titanium alloy is hot forged before the hot-compression experiments in this work, and the large bulk α phase in Fig. 1 is the residual microstructure of the original titanium alloy bar.

However, when the alloy is deformed to 0.22, the tiny lamellar α phases in the as-received alloy are dissolved into the β matrix, and the microstructure consists of the equiaxed and some lamellar α phases, Fig. 2a–c. Generally, when the titanium alloy deforms at the $\alpha+\beta$ phase zone, although the β transition temperature is higher than the deformation temperature, the $\alpha \rightarrow \beta$ DPT still occurs, and some phases with a large diameter will grow at high deformation temperatures due to the Ostwald ripening effect [48–50]. In the TMP process, the proliferation and entanglement of dislocations increase the deformation storage energy, which favors the DPT. Therefore, only equiaxed and some large lamellar α phases can be found in Fig. 2a. The diameter of the equiaxed α phase with a fraction of 46.1 % is 5.14 μm, and the thickness and fraction of the lamellar α phase are 0.80 μm and 10.2 %, respectively, Figs. 2b,c,j,k. Meanwhile, due to the DPT, the diameter of the equiaxial phase and the thickness of the lamellar phase are increased when compared with those of the as-received alloy in Fig. 2j.

With the true strain increasing to 0.51, i.e., the engineering strain is 0.4, some lamellar α phases are transformed into small equiaxed α phases, and the thickness of the lamellar α phases is decreased, as shown in Figs. 2d–f. Due to the DRX of the large equiaxed α phases and the dynamic globalization, a portion of small equiaxed α phases is observed in Figs. 2d–f. Therefore, the average diameter of the equiaxed α phase is decreased. The diameter of the equiaxed α phase with a fraction of 45.6 % is 3.65 μm, and the thickness and fraction of the lamellar α phase are 0.68 μm and 15.5 %, respectively, Figs. 2e,f,j,k. However, when the strain is further increased to 0.92, the α phases exhibit large equiaxed and thick lamellar morphologies, Figs. 2g–i, and the diameter of equiaxed α phase with a fraction of 35.0 % is 4.10 μm, and the thickness and fraction of lamellar α phase are 0.94 μm and 13.3 %, respectively, Figs. 2h,i,j,k, indicating that the lamellar α phase is thickened.

Figure 2l shows the microhardness of the studied alloy deformed at 1173 K, 0.1 s^{-1}, and different true strains. The microhardnesses are 336.1, 357.4, and 322.4 HV at true strains of 0.22, 0.51, and 0.92, respectively. With the increase of strain, the microhardness increases and then decreases; the spheroidization effect of the lamellar α phase is evident, resulting in the formation of some fine equiaxed α phases at the true strain of 0.22 and 0.51, as shown in Figs. 2a,d. The fine equiaxed α phases can act as hard particles, strengthening the alloy and increasing its microhardness. With the true strain increasing to 0.92, the α phases are in the form of large equiaxed and thick lamellar morphologies; the fine equiaxed α phases are dissolved, Fig. 2g, and the microhardness decreases.

As shown in Fig. 3, a similar phenomenon is observed at a relatively low deformation temperature (1093 K, 0.1 s^{-1}). When the true strain is 0.22, a plentiful of tiny lamellar α phases can be found, and the degree of dissolution of the tiny lamellar α phases is decreased when compared with that at 1173 K, Figs. 2a–c and Figs. 3a–c. The dimensions of the equiaxial and lamellar phases at a true strain of 0.22 are 3.50 and 0.50 μm, while the fractions are 33.6 and 11.6 %, respectively, Figs. 3b,c,j,k. Increasing the true strain to 0.92, the fraction of α phase is decreased to 41.3 %, and the average dimension of the equiaxial α phase is further decreased to 3.41 μm, Figs. 3j,k. Due to the low deformation temperature, the thickness variation of the lamellar α phases is less pronounced than at 1173 K. However, the average dimension of the α phase first increases and then decreases.

Therefore, it can be concluded that the lamellar and equiaxed α phases will undergo distinct evolution mechanisms, and that the TMP parameters have a significant effect on the α-phase evolution mechanism [51, 52]. For the equiaxed phase, the $\alpha \rightarrow \beta$ DPT, the Ostwald ripening effect, and the lamellation can occur due to the coupled deformation process. As shown in

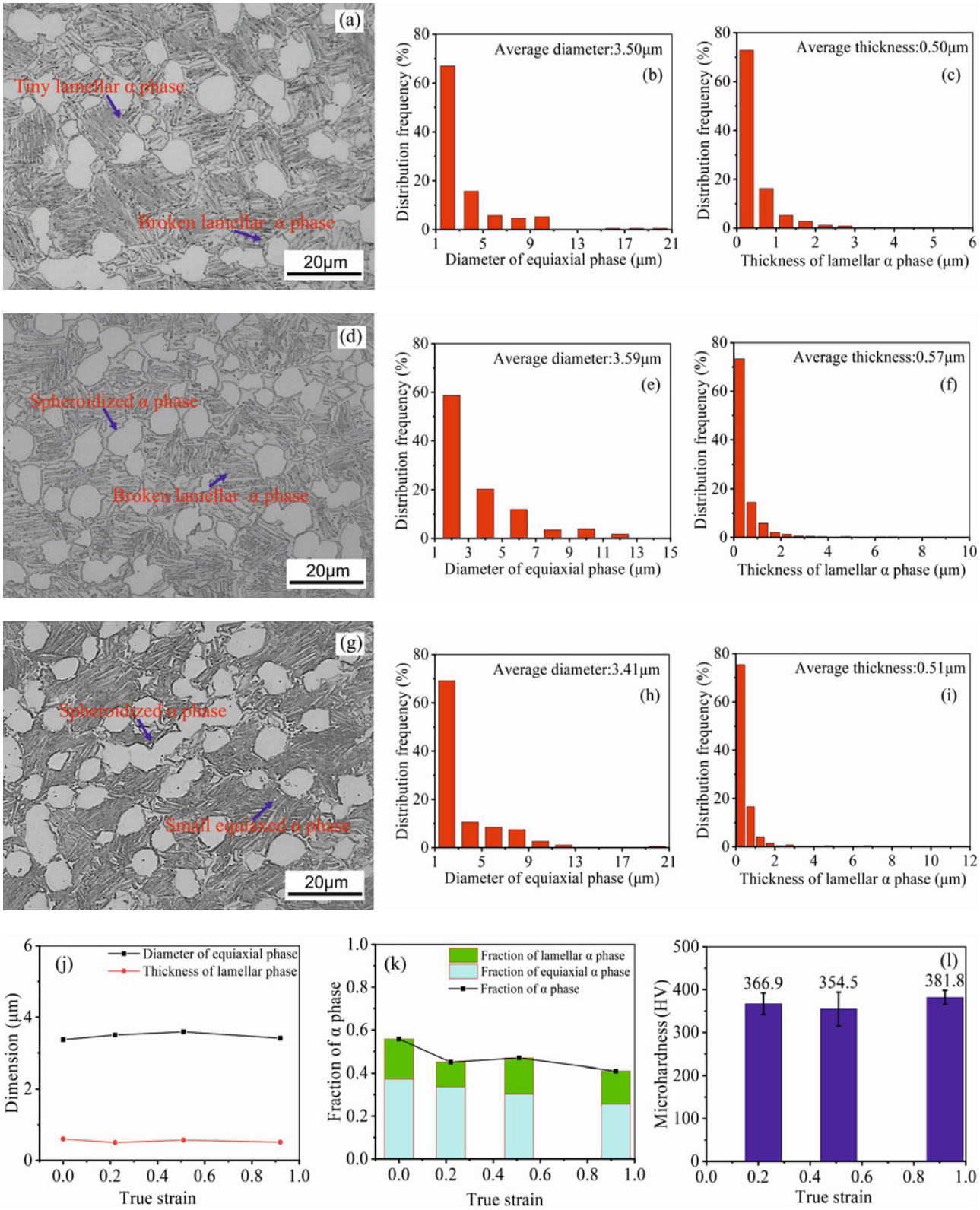

Fig. 3. The OM of the alloy deformed at 1093 K, 0.1 s^{-1} and true strain of: (a)–(c) 0.22, (d)–(f) 0.51, (g)–(i) 0.92, (j) dimension of α phase, (k) fraction of α phase, and (l) microhardness.

Figs. 1a and 2a, when the alloy is deformed at a relatively high temperature, i.e., 1173 K, the tiny equiaxed α phases are dissolved at the beginning of the hot deformation, and the average diameter of the equiaxed α phases is increased. Then, when the strain is increased, the spheroidization of lamellar α phases takes place,

and some tiny equiaxed α phases are formed, leading to the decreased average diameter of the equiaxed α phases. However, with further increased strain, a portion of the equiaxed α phases grows, and their diameter increases, Figs. 2d–i. In contrast, the growth and dissolution of the tiny equiaxed α phases are not obvious at a relatively low deformation temperature, i.e., 1093 K (Fig. 3).

As for the lamellar α phases, spheroidization, Ostwald ripening, and DPT may occur simultaneously. Due to the relatively high temperature, the small lamellar α phases are rapidly dissolved into the β matrix at a true strain of 0.22, resulting in the increased thickness of lamellar α phases, Fig. 2a. Compared with the large lamellar α phases, the small lamellar α phases are more prone to spheroidization. At a true strain of 0.51, because of the large deformation, the DPT occurs, and the size of the lamellar α phases decreases slightly, Fig. 2j. When the true strain is further increased to 0.91, the deformation energy also increases, and the transformation and spheroidization of the thin lamellar phases are more complete, leading to an increased thickness of the lamellar phase. However, at the relatively low deformation temperature, the growth of the lamellar phase is inhibited. Upon the deformation initiation, the small lamellar phases are partly dissolved, and the average thickness decreases, Fig. 3a. As the small lamellar phase is sufficiently dissolved, the average lamellar thickness increases at a true strain of 0.51, Fig. 3d. Subsequently, the thicker lamellar phases are also dissolved, and the thickness continues to decrease, Fig. 3g.

The α-phase fraction and the equiaxed phase both vary with the true strain. At a relatively high deformation temperature, the small α phase dissolves and the large α phase grows, and the total fraction of the α phase constantly rises, Fig. 2k. This phenomenon can also be seen from the proportion distribution in Figs. 1–3. During the deformation, the lamellar α phase continuously spheroidizes, the small equiaxed α phase grows simultaneously, and the fraction continues to increase at a true strain of 0.51. Subsequently, the temperature rises significantly due to the large deformation, the DPT intensifies, and the fraction of the α phase decreases, Fig. 2k. At a low temperature, the growth is not obvious, and the fraction of the α phase decreases. Then, the spheroidized equiaxed phase grows at 0.51, the fraction of the α phase increases, and, finally, as the temperature rises, the total fraction of the α phase decreases (Fig. 3k). In the TMP, the DPT and deformation occur simultaneously. As the lamellar α phase becomes spherical, the spherical α phase undergoes deformation and transforms into the tiny lamellar α phase again, leading to a continuous increase in the proportion of the lamellar α phase and a continuous decrease in the proportion of the equiaxed α phase, as shown in Figs. 2k and 3k.

Figure 3l shows the microhardness of the studied alloy deformed at 1093 K and 0.1 s^{-1}, for different true strains. The micro hardnesses are 366.9, 354.5, and 381.8 HV at 0.22, 0.51, and 0.92, respectively. Compared to 1173 K, the hardness is increased. Due to the restriction of DPT and DRX at low temperatures, significant material softening does not occur. With increasing strain, the microhardness decreases, then increases. At the beginning of deformation, some small lamellar α phases can hinder the dislocation movement. Increasing the true strain to 0.51, the small lamellar α phase is sufficiently dissolved, and the hardness begins to decrease. Further increasing the true strain to 0.92, the thicker lamellar α phases are also dissolved, the spheroidization effect increases, and the fine equiaxed α phase is formed. The fine equiaxed α phase can hinder dislocation movement, leading to increased hardness.

3.2. Effect of deformation temperature

Figure 4 shows the OM of the alloy deformed at a strain rate of 0.1 s^{-1}, a strain of 60 %, and different deformation temperatures. It can be found in the Figs. 2–4 that the microstructures are remarkably affected by the deformation temperature. At a relatively low deformation temperature (1093, 1133, and 1173 K), the microstructure mainly consists of equiaxed and lamellar α phases. In comparison, only equiaxed α phase and some incomplete β grain boundaries are observed at 1213 K (Figs. 4d–f). The equiaxial α phase maintains its morphology after hot deformation, and hot deformation has little effect on its shape. It can be observed that with the increased temperature, there is little variation in the morphology of equiaxed α phases, and the morphology and fraction of lamellar α phases are significantly changed, especially at 1213 K, Figs. 4d–f, the lamellar α phases have almost disappeared. These phenomena indicate that the lamellar α phase and β phase undergo the main deformation, while the equiaxial α phase remains undeformed during the high-temperature deformation process. This is correlated to the crystal structure of the α and β phases. Generally, the BCC-structured β phase has more slip systems, plastic deformation preferentially occurs in the β phase, and the HCP-structured equiaxial α phase can rotate to coordinate with the macroscopic deformation of the alloy [53]. Due to the relatively large aspect ratio of the lamellar α phase, deformation instability is easy to occur, and the lamellar α phase is readily cut off by dislocations, leading to fragmentation and spheroidization.

The dimensions of the equiaxial α phase after deformation at 1093, 1133, 1173, and 1213 K are 3.41, 3.33, 4.10, and 4.67 μm, respectively, Figs. 4g,h. When the deformation temperature rises from 1093 to 1133 K, the size of the equiaxed α phase is almost

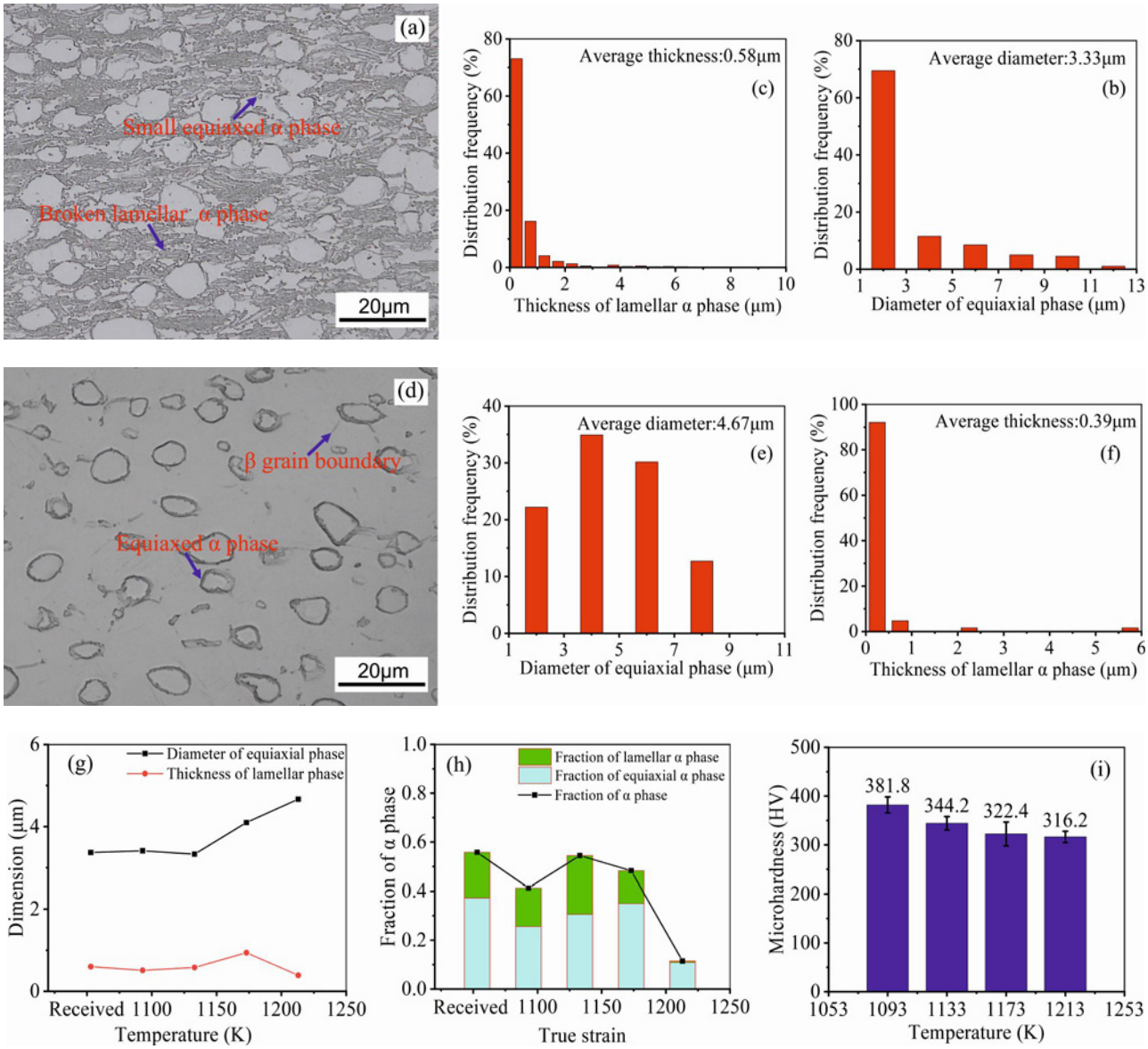

Fig. 4. The OM of the studied alloy deformed at a strain rate of 0.1 s^{-1}, strain of 60 %, and temperature of: (a)–(c) 1133 K, (d)–(f) 1213 K, (g) dimension of α phase, (h) fraction of α phase, and (i) microhardness.

unchanged. This phenomenon can be ascribed to the spheroidization and DPT of the small α phase. During high-temperature deformation, the tiny α phase, a part of the lamellar α phase, is spherized, and a new tiny α phase forms again. As a result, the size of the equiaxial α phase is almost unchanged. However, the DPT is accelerated, the tiny α phase is changed into β phase, the larger α phase is preserved in the matrix, and the size of the equiaxial α phase is raised at 1173 and 1213 K, Figs. 2l and 4g. At 1093, 1133, 1173, and 1213 K, the average thickness of the lamellar α phase is 0.51, 0.58, 0.94, and 0.39 μm, respectively (Figs. 2g, 3g, and 4g). The average thickness is slightly increased at low deformation temperature. At 1173 K, the tiny lamellar α phase is quickly converted into β phase, and the thickness of the lamellar α phase is raised. However, due to the relatively high temperature of 1213 K, the DPT is evident, resulting in a decreased thickness.

As shown in Figs. 2k, 3k, and 4h, the fractions of α phases are 41.3, 54.4, 48.3, and 11.5 % at 1093, 1133, 1173, and 1213 K, and the fractions of equiaxed α phases are 25.6, 30.6, 35.0, and 10.9 %, respectively. At a low deformation temperature, such as 1093 K, the DPT and precipitation of α phase occur simultaneously, and the total fraction of α phase and the equiaxed α phase decrease, mainly caused by the DPT of small-sized equiaxed and lamellar α phases. When the deformation temperatures are increased to 1133 and 1173 K, the spheroidization process accelerates, and a fine, equiaxed α phase forms. Due to the high temperature, a part of the fine equiaxed α phase is dissolved, while another part of the fine equiaxed α phase

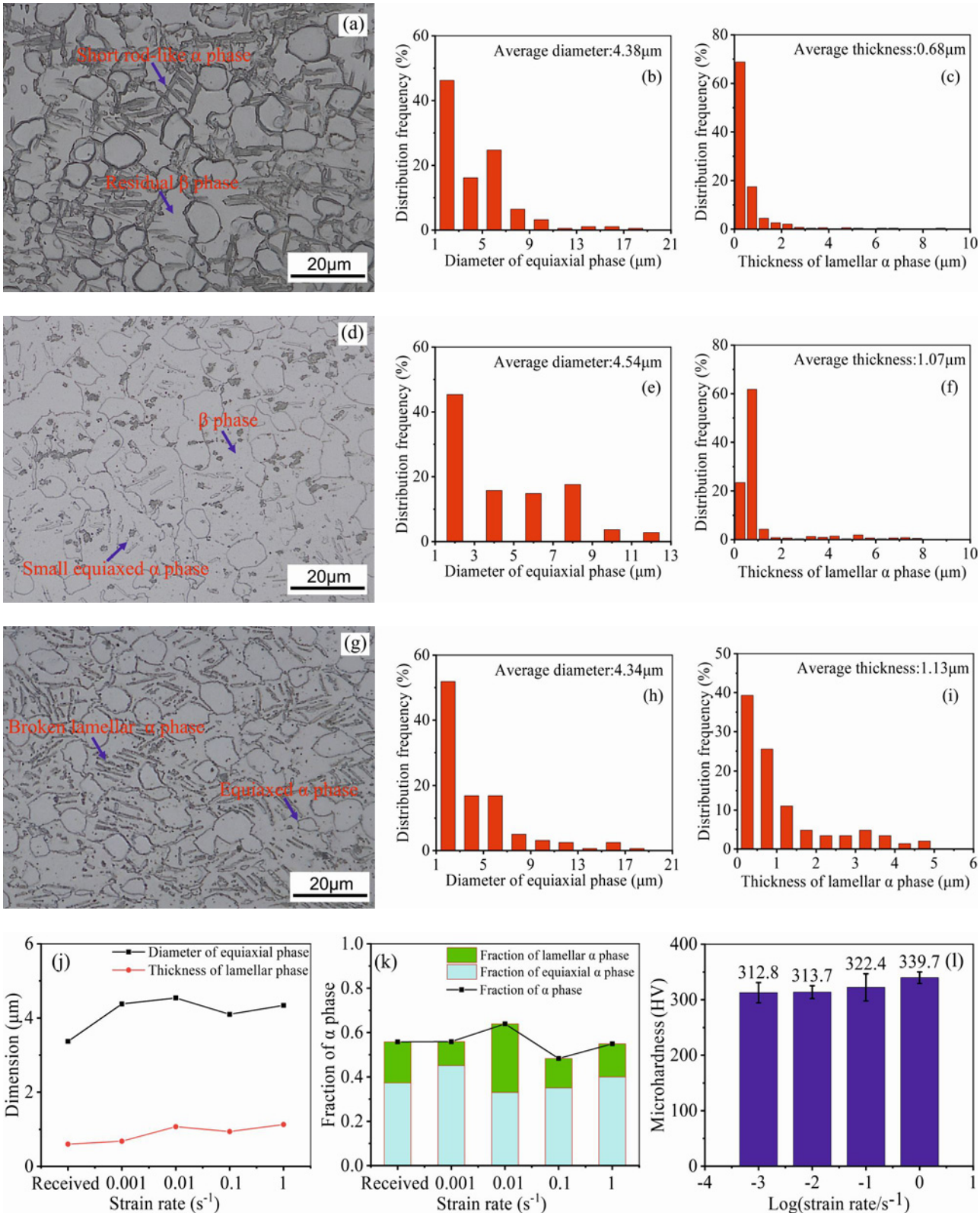

Fig. 5. OM of the alloy deformed at 1173 K, strain of 60 %, strain rates of: (a)–(c) 0.001 s^{-1}, (d)–(f) 0.01 s^{-1}, (g)–(i) 1 s^{-1}, (j) dimension of α phase, (k) fraction of α phase, and (l) microhardness.

absorbs the surrounding solute atoms and grows, and the fraction of the total α phase and the equiaxed α phase is increased. However, at 1213 K, strong DPT occurs, the lamellar α phase almost disappears, and

the fraction of α phase and the equiaxed α phase decreases. Figure 4i shows the microhardness of the alloy deformed at a strain rate of $0.1\,s^{-1}$, strain of 60 %, and different deformation temperatures. The micro hardnesses are 381.8, 344.2, 322.4, and 316.2 HV at 1093, 1133, 1173, and 1213 K, respectively. As the deformation temperature increases, the accelerated dynamic phase transformation makes the harder α phase transform into the β phase. The α phase has an HCP structure, which can effectively hinder dislocation motion within the alloy. The β phase has a BCC structure and is less resistant to deformation than the α phase, leading to a decrease in the alloy's hardness at high deformation temperatures.

3.3. Effect of strain rate

Figures 2g–i and Fig. 5 are the OM of the studied alloy deformed at 1173 K, strain of 60 %, and various strain rates. It can be found in the Figs. 2g–i and Fig. 5 that the microstructure of the studied alloy is mostly constituted of equiaxial and residual lamellar α phases.

As the strain rate is $0.001\,s^{-1}$, the average diameter of equiaxial and thickness of lamellar α phase are 4.38 μm and 0.68 μm, Figs. 5a–c,j,k. Due to the low strain rate and high deformation temperature, there is enough time for the evolution of the α phase, the tiny α phase is converted into β phase, and some lamellar α phase is thickened, leading to the formation of short rod-like α phase, Fig. 5a. The grown-up of the large equiaxial α phase and the DPT of tiny phases occur at the same time, the fraction of the α phase is almost unchanged. However, the fraction of the lamellar α phase is remarkably decreased, Figs. 5j,k. When the studied alloy is deformed at a relatively high strain rate, such as $0.1\,s^{-1}$, because of the constrained deformation time, the DPT and the spheroidization are insufficient, the average diameter is decreased, and the thickness is increased, Figs. 2g–i. At a strain rate of $1\,s^{-1}$, there are fewer spheroidized α phases at the increased strain rate, and the formation of a very fine equiaxial α phase is blocked, Figs. 5g–i. Therefore, the average diameter and the fraction of the α phase increase.

Figure 5l shows the microhardness of the studied alloy deformed at 1173 K, 60 % strain, and various strain rates. The microhardness is 312.8, 313.7, 322.4, and 339.7 HV at strain rates of 0.001, 0.01, 0.1, and $1\,s^{-1}$, respectively. With increasing strain rate, the microhardness gradually increases. Due to higher strain rates and WH, dislocation entanglement is more pronounced, and dislocation density is higher at higher strain rates. At the same time, the deformation time is relatively short, and the grain growth time during DRX is insufficient, resulting in grain refinement and increased hardness.

4. Constitutive modeling

4.1. Hot deformation behavior

Figure 6 presents the true stress-strain of the studied alloy, as reported in the previous work [46]. The true stress increases significantly with the true strain until reaching a maximum, then gradually decreases with continued strain, and finally stabilizes into a steady-state condition. In the initial stage of high-temperature deformation, dislocations in the alloy multiply, and the WH rate increases rapidly, leading to a maximum flow stress. As high-temperature deformation continues, DRV and DRX form, and the true stress decreases. When the WH rate and DRV/DRX softening rate reach an equilibrium, the hot deformation enters the steady-state stage.

4.2. Arrhenius constitutive equation

The relationship among deformation temperature, strain rate, and flow stress in the high-temperature deformation can be provided as:

$$\dot{\varepsilon} = A_1 \sigma^{n_1} \exp\left(-\frac{Q}{RT}\right), \ as < 0.8, \tag{1}$$

$$\dot{\varepsilon} = A_2 \exp(\beta\sigma) \exp\left(-\frac{Q}{RT}\right), \ as < 1.2, \tag{2}$$

$$\dot{\varepsilon} = A\left[\sinh(\alpha\sigma)\right]^n \exp\left(-\frac{Q}{RT}\right), \text{all stress values}, \tag{3}$$

where $\dot{\varepsilon}$ represents the strain rate, σ represents the stress value, Q stands for the hot deformation activation energy ($kJ\,mol^{-1}$), R is the molar gas constant ($8.314\,J\,mol^{-1}\,K^{-1}$), and T represents the deformation temperature (Kelvin temperature). A_1, n_1, A_2, β, A, α, and n are material-related parameters. The correlation between α and β can be shown as: $\alpha = \beta/n_1$.

During the hot deformation, the strain rate and deformation temperature can also be provided as:

$$Z = \dot{\varepsilon} \exp\left(-\frac{Q}{RT}\right), \tag{4}$$

where Z represents the Zener-Hollomon parameter. Combining Eqs. (3) and (4), the relationship between Z and stress can be derived:

$$Z = A\left[\sinh(\alpha\sigma)\right]^n. \tag{5}$$

Therefore, the flow stress σ can be derived through:

$$\sigma = \frac{1}{\alpha}\ln\left\{\left[\frac{\dot{\varepsilon}\exp\left(\frac{Q}{RT}\right)}{A}\right]^{\frac{1}{n}} + \left[\left[\frac{\dot{\varepsilon}\exp\left(\frac{Q}{RT}\right)}{A}\right]^{\frac{2}{n}} + 1\right]^{\frac{1}{2}}\right\}. \tag{6}$$

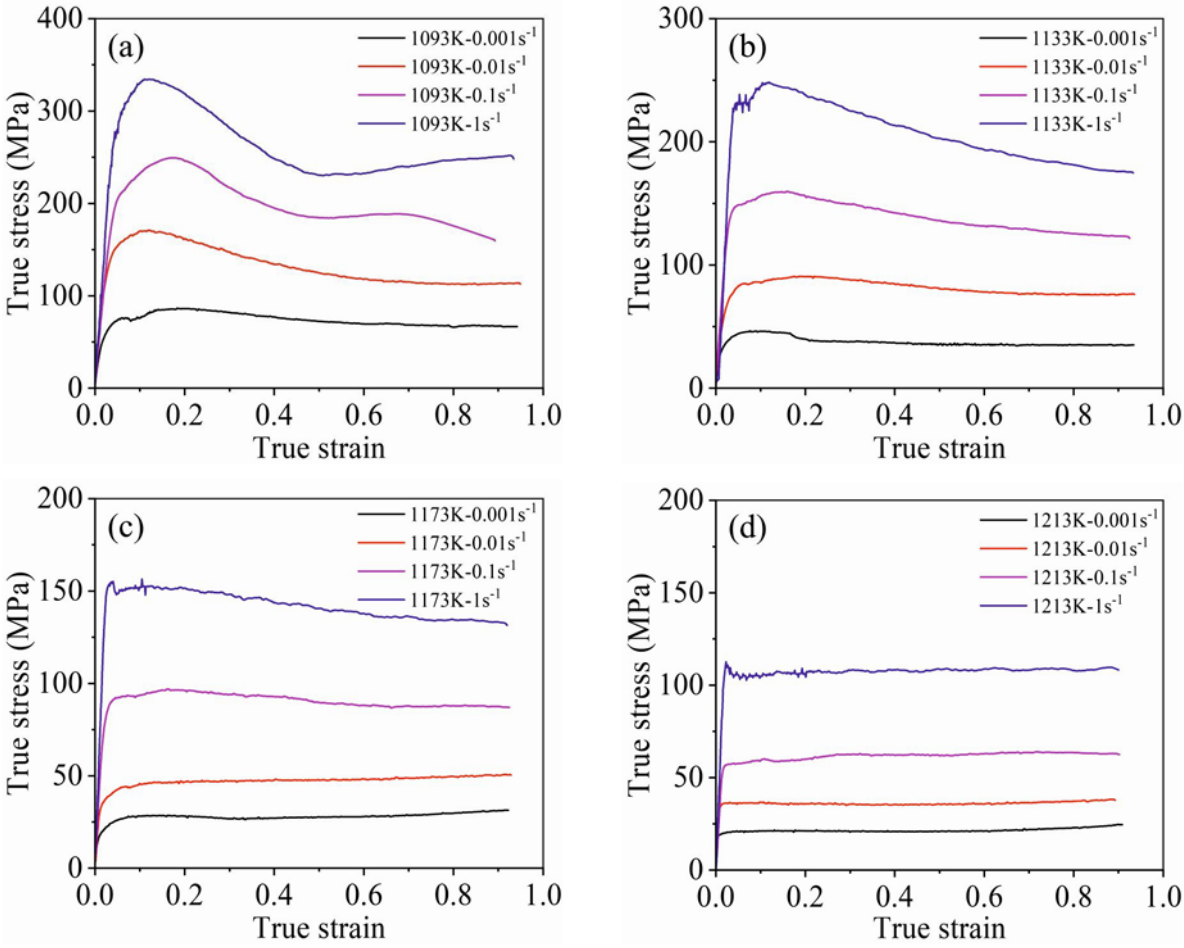

Fig. 6. The studied alloy true stress-strain curve at (a) 1093 K, (b) 1133 K, (c) 1173 K, and (d) 1213 K.

4.2.1. Determination of the α values

Applying the natural logarithm of Eqs. (1) and (2) yields:

$$\ln \dot{\varepsilon} = \ln A_1 + n_1 \ln \sigma - \frac{Q}{RT}, \tag{7}$$

$$\ln \dot{\varepsilon} = \ln A_2 + \beta\sigma - \frac{Q}{RT}. \tag{8}$$

Taking the partial derivatives of Eqs. (4) and (5) yields:

$$n_1 = \frac{\partial (\ln \dot{\varepsilon})}{\partial (\ln \sigma)}, \tag{9}$$

$$\beta = \frac{\partial (\ln \dot{\varepsilon})}{\partial \sigma}. \tag{10}$$

At a constant temperature, the mean slope values for ln-lnσ and ln-σ correspond to the values of n_1 and β. Substituting the stress-strain at a true strain of 0.4 into Eqs. (7) and (8), Fig. 7 shows the relationship between ln-lnσ and ln-σ plotted.

Table 1 shows the values of n_1 and β at different deformation temperatures.

Table 1. The values of n_1, β, and α at different temperatures

T (K)	n_1	β	$\alpha = \beta/n_1$
1093	5.7315	0.0401	0.0070
1133	3.8649	0.0389	0.0101
1173	4.0274	0.0566	0.0141
1213	4.1876	0.0752	0.0180

4.2.2. Determination of the n values

Taking the natural logarithm of Eq. (3) yields:

$$\ln \dot{\varepsilon} = \ln A + n \ln [\sinh (\alpha\sigma)] - \frac{Q}{RT}. \tag{11}$$

Applying the partial derivatives of Eq. (8) with respect to ln[sinh($\alpha\sigma$)] gets:

$$n = \frac{\partial \ln \dot{\varepsilon}}{\partial [\ln \sinh (\alpha\sigma)]}. \tag{12}$$

So, when the temperature is constant, the parameter n represents the slope of the ln-ln[sinh($\alpha\sigma$)] curve.

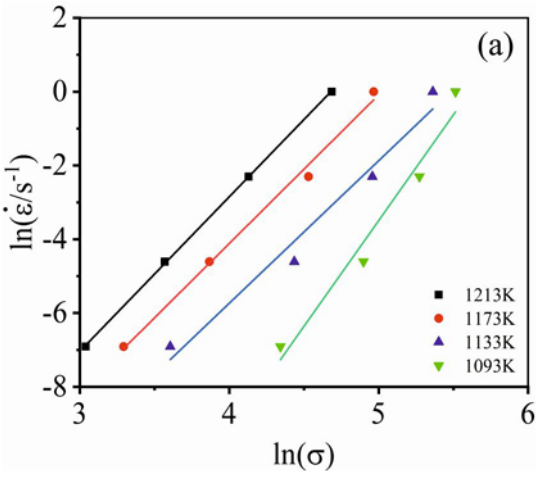

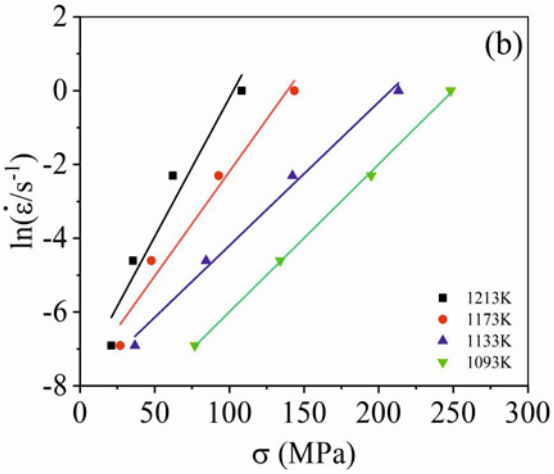

Fig. 7. Linear relationships of (a) $\ln\dot{\varepsilon}$-$\ln\sigma$ and (b) $\ln\dot{\varepsilon}$-σ.

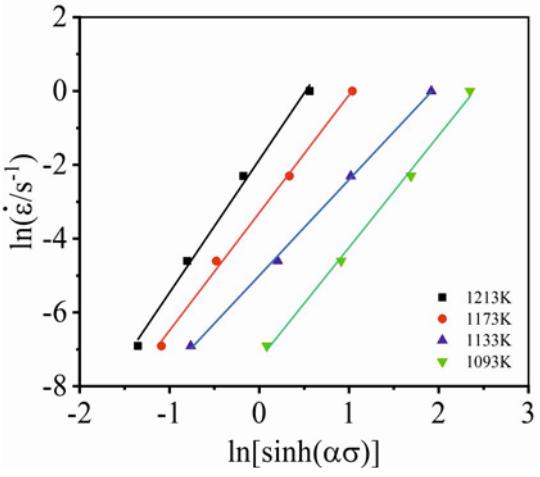

Fig. 8. The linear relationships between $\ln\dot{\varepsilon}$ and $\ln[\sinh(\alpha\sigma)]$. $\ln[\sinh(\alpha\sigma)]$ is plotted, as shown in Fig. 8.

Substituting the stress-strain at true strain of 0.4 into Eq. (11), the relationship between ln and $\ln[\sinh(\alpha\sigma)]$ is plotted as shown in Fig. 8.

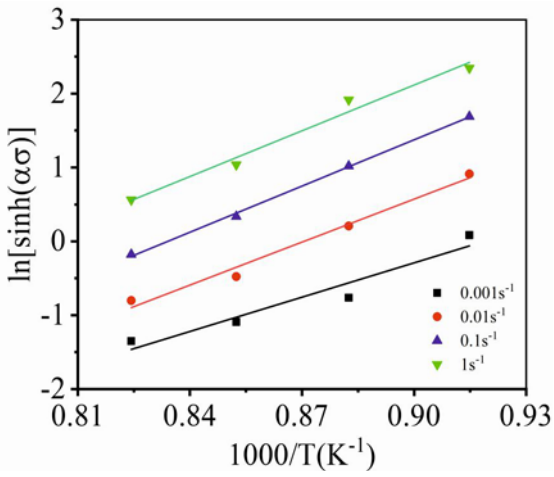

Fig. 9. The linear relationships between $\ln[\sinh(\alpha\sigma)]$ and $1/T$.

4.2.3. Determination of the Q values

Equation (8) can be transformed into:

$$\ln\left[\sinh\left(\alpha\sigma\right)\right] = \ln\dot{\varepsilon}/n - \ln A/n + \frac{Q}{nRT}. \tag{13}$$

Taking the partial derivatives of Eq. (13) with respect to $1/T$ gets:

$$\frac{Q}{nR} = \frac{\partial \ln\left[\sinh\left(\alpha\sigma\right)\right]}{\partial\left(1/T\right)}. \tag{14}$$

When the strain rate is constant, the activation energy Q can be determined by calculating the slope of the $\ln[\sinh(\alpha\sigma)]$-$1/T$ curve, then substituting the values of n and R into the corresponding equation. Figure 9 shows the relationship between $\ln[\sinh(\alpha\sigma)]$ and $1/T$, and the average value of Q is 487.5443 kJ mol^{-1}. Generally, the material parameters, such as the activation energy Q, are related to the DRV and DRX processes. In the DRV process, the activation energy Q is close to the self-diffusion activation energy of materials, while the DRX is accompanied by the formation of sub-grains and the migration of large-angle grain boundaries, and the Q is larger than the self-diffusion activation energy. The self-diffusion activation energy of α-Ti is 169 kJ mol^{-1} and 153 kJ mol^{-1} for β-Ti [54]. Figure 9 reveals that the value of Q is 487.5443 kJ mol^{-1}, which is larger than the self-diffusion activation energy, suggesting the DRX is a major softening mechanism of the studied alloy.

4.2.4. Determination of the Z values

Applying the natural logarithm of Eq. (5) yields:

$$\ln Z = \ln A + n\ln\left[\sinh\left(\alpha\sigma\right)\right]. \tag{15}$$

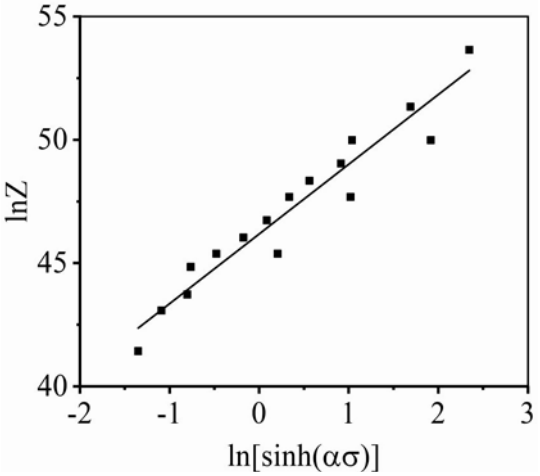

Fig. 10. Relationships between $\ln Z$ and $\ln[\sinh(\alpha\sigma)]$.

Substituting the strain rate, deformation temperature, and Q into Eq. (4), the Z value can be obtained. The $\ln Z$-$\ln[\sinh(\alpha\sigma)]$ curve in Fig. 10 can be plotted using Eq. (15), and the intercept of the curve corresponds to $\ln A$. The value of A is 1.13903×10^{20}.

Substituting the parameters obtained from the above calculations into Eq. (3), the Arrhenius constitutive equation for the studied titanium alloy can be established at a true strain of 0.4:

$$\dot{\varepsilon} = 1.1390 \times 10^{20} \left[\ln \sinh \left(0.0123\sigma\right)\right]^{3.107} \cdot 6 \exp\left(-\frac{487.5443 \times 10^3}{8.314T}\right). \quad (16)$$

Inserting the parameters into Eq. (6), the flow stress of the studied titanium alloy at a true strain of 0.4 can be expressed as:

$$\sigma = 81.54 \ln \left\{ \left[\frac{\dot{\varepsilon} \exp\left(\frac{487544.3}{8.314T}\right)}{1.1390 \times 10^{20}}\right]^{0.3218} + \left[\left[\frac{\dot{\varepsilon} \exp\left(\frac{487544.3}{8.314T}\right)}{1.1390 \times 10^{20}}\right]^{0.6436} + 1\right]^{\frac{1}{2}} \right\}. \quad (17)$$

Table 2. Material parameters under different strains

ε	α	n	Q	$\ln A$
0.1	0.0114	2.9484	566.3584	54.3033
0.2	0.0116	2.9620	552.7427	52.8354
0.3	0.0119	2.9982	522.0714	49.7044
0.4	0.0127	3.1076	487.5443	46.1819
0.5	0.0125	3.1751	461.5903	43.5518
0.6	0.0126	3.1776	452.7204	42.6354
0.7	0.0126	3.2003	447.9726	42.1437
0.8	0.0126	3.2591	435.2679	40.8616
0.9	0.0124	3.3643	429.4418	40.3297

It is observed from Eq. (17) that the flow stress is determined by strain rate and deformation temperature. Different strain conditions lead to variations in flow stress. Therefore, the flow stress also depends on strain.

4.2.5. Strain compensatory Arrhenius model

The model parameters at a true strain of 0.4 can be determined in Section 4.2.1. Following the same approach, the parameters under other strain conditions can be obtained, as presented in Table 2.

The parameters in Table 2 can be expressed as a function of strain, and the 5th polynomial fitting is best to describe this relation, as illustrated in Fig. 11. The factors in the 5th polynomial fitting are listed in Eq. (18) and Table 3.

$$\begin{bmatrix} \alpha(\varepsilon) \\ n(\varepsilon) \\ Q(\varepsilon) \\ \ln A(\varepsilon) \end{bmatrix} = \begin{bmatrix} X_0 & X_1 & X_2 & X_3 & X_4 & X_5 \\ Y_0 & Y_1 & Y_2 & Y_3 & Y_4 & Y_5 \\ U_0 & U_1 & U_2 & U_3 & U_4 & U_5 \\ V_0 & V_1 & V_2 & V_3 & V_4 & V_5 \end{bmatrix} \begin{bmatrix} 1 \\ \varepsilon \\ \varepsilon^2 \\ \varepsilon^3 \\ \varepsilon^4 \\ \varepsilon^5 \end{bmatrix}. \quad (18)$$

where ε represents the strain, and X_i, Y_i, U_i, and V_i represent the coefficients.

Substituting Eq. (18) into Eq. (6), the strain com-

Table 3. The fitting coefficients of α, n, Q, and $\ln A$

α	n	Q	$\ln A$
$X_0 = 0.0117$	$Y_0 = 3.1447$	$U_0 = 508.6163$	$V_0 = 48.6139$
$X_1 = -0.0061$	$Y_1 = -3.3597$	$U_1 = 1128.4899$	$V_1 = 111.8952$
$X_2 = 0.0444$	$Y_2 = 17.1570$	$U_2 = -6849.3738$	$V_2 = -686.5431$
$X_3 = -0.0922$	$Y_3 = -30.8307$	$U_3 = 14179.6998$	$V_3 = 1426.5725$
$X_4 = 0.0830$	$Y_4 = 22.7968$	$U_4 = -12855.5430$	$V_4 = -1297.6322$
$X_5 = -0.0289$	$Y_5 = -5.3059$	$U_5 = 4318.7967$	$V_5 = 437.6827$

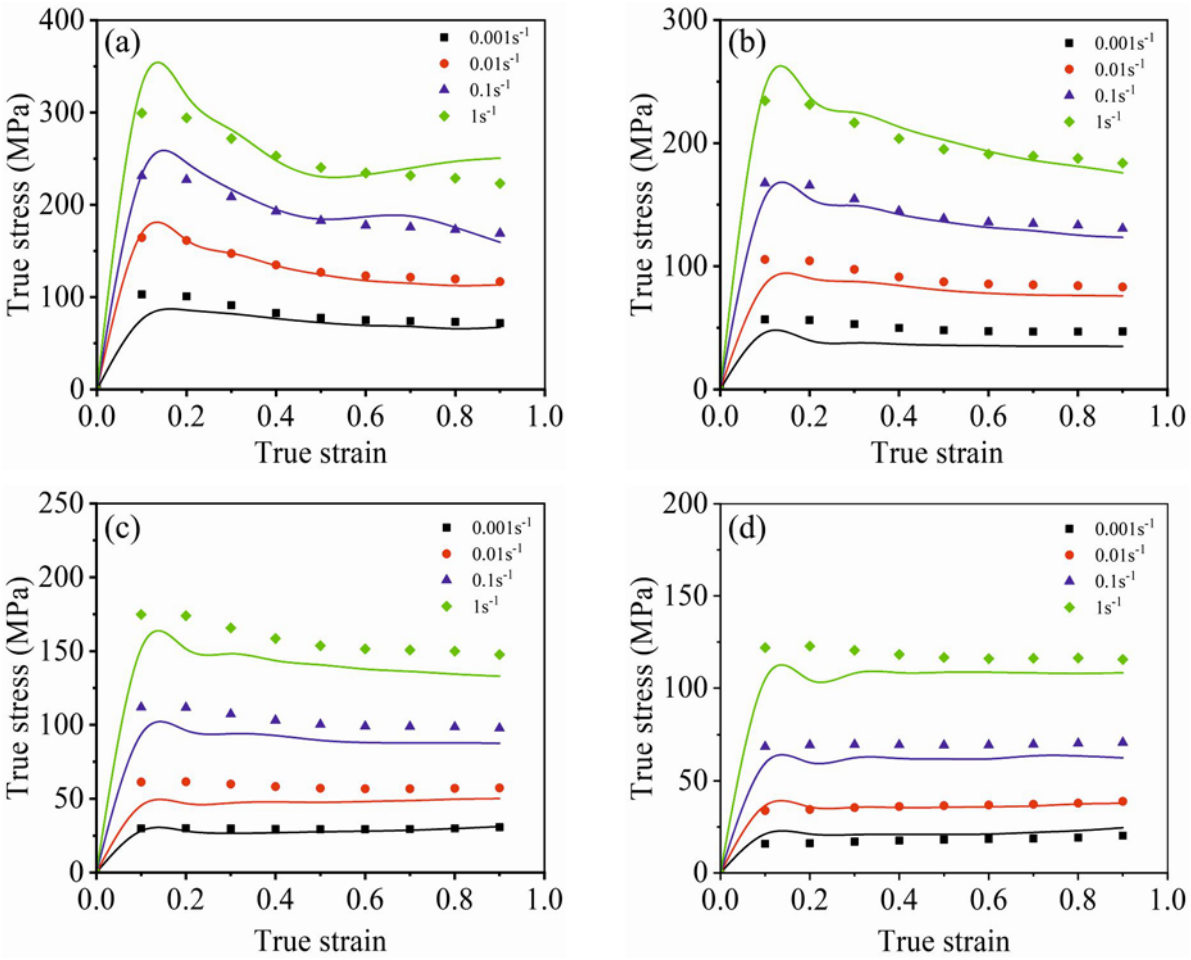

Fig. 11. Polynomial fittings of (a) α , (b) n, (c) Q, and (d) $\ln A$.

pensatory Arrhenius model can be obtained:

$$\sigma = \frac{1}{\alpha(\varepsilon)} \ln \left\{ \left[\frac{Z(\varepsilon)}{A(\varepsilon)} \right]^{\frac{1}{n(\varepsilon)}} + \left[\left[\frac{Z(\varepsilon)}{A(\varepsilon)} \right]^{\frac{2}{n(\varepsilon)}} + 1 \right]^{\frac{1}{2}} \right\}, \tag{19}$$

$$Z = \dot{\varepsilon} \exp\left(\frac{Q(\varepsilon)}{RT} \right). \tag{20}$$

Figure 12 shows the comparisons of the predicted and experimental stress value of the strain-compensated constitutive model, the correlation coefficient R, and the average absolute relative error ($AARE$) in Eqs. (21) and (22) are used to evaluate the correctness of the established model.

$$R = \frac{\sum_{i=1}^{n} \left[\left(E_i - \bar{E} \right) \left(P_i - \bar{P} \right) \right]}{\sqrt{\sum_{i=1}^{n} \left(E_i - \bar{E} \right)^2} \sqrt{\sum_{i=1}^{n} \left(P_i - \bar{P} \right)^2}}, \tag{21}$$

$$AARE = \frac{1}{n} \sum_{i=1}^{n} \left| \frac{E_i - P_i}{E_i} \right| \times 100\%, \tag{22}$$

where n represents the number of data, E_i represents the experimental value, P_i represents the predicted value, $\bar{E}$ and $\bar{P}$ are the average values of E_i and P_i, respectively. The values of R and $AARE$ are 0.0809 and 0.9848, indicating the good prediction ability of the established model.

5. Conclusions

In this paper, the microstructure characteristics and high-temperature deformation response of a Ti-6Al-2Sn-2Zr-3Mo-1Cr-2Nb titanium alloy were studied, and a strain-compensated Arrhenius constitutive model was developed. The main conclusions are as follows:

(1) The equiaxial α phase still shows the equiaxial morphology after hot deformation, and hot deformation has little influence on the shape of the equiaxial α phase. The size and fraction of the α phase vary with the hot-deformation parameters.

(2) The true strain, deformation temperature, and strain rate have an enormous effect on the microstruc-

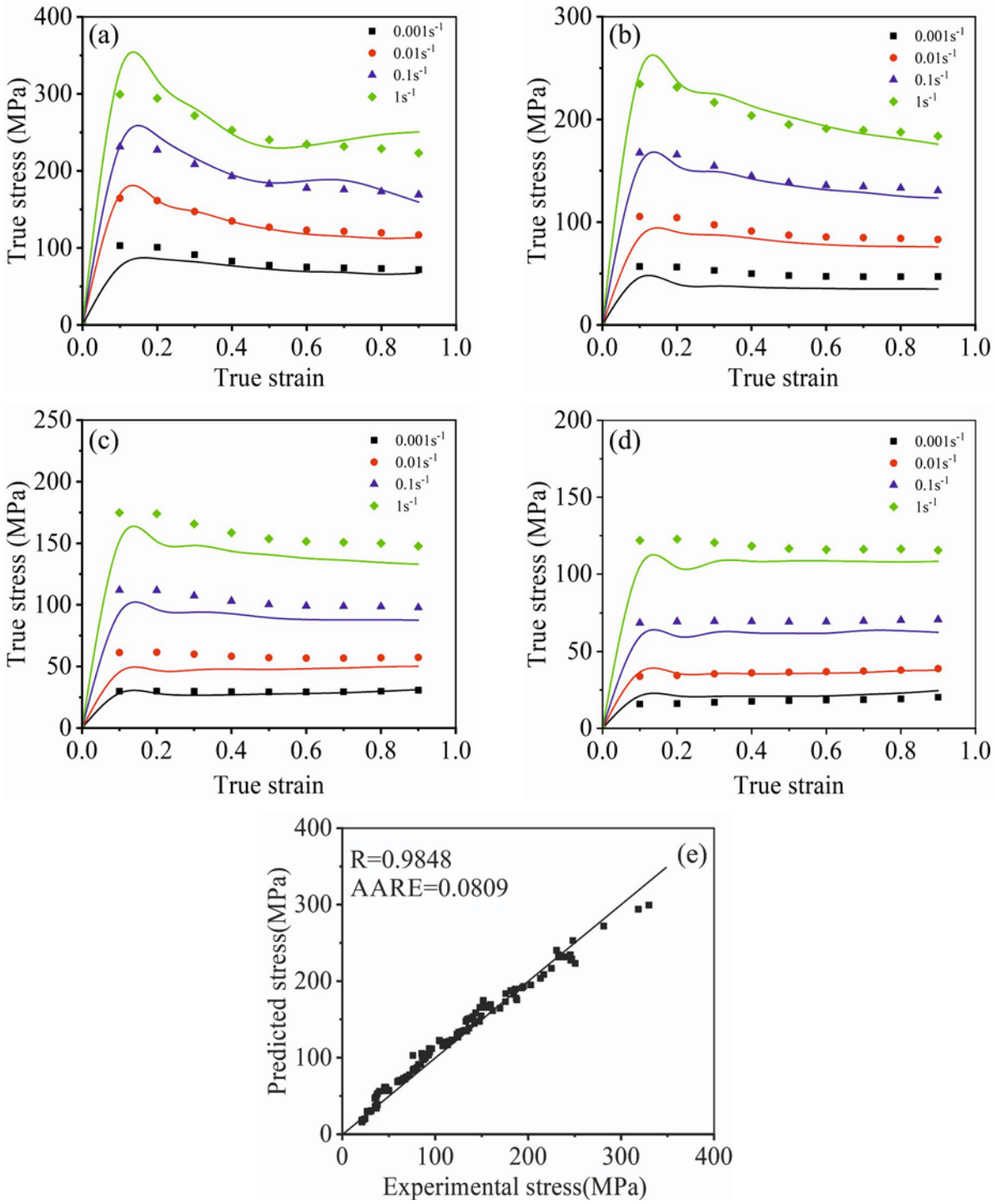

Fig. 12. Comparisons between predicted (point) and experimental (line) stress for studied titanium alloy: (a) 1093 K, (b) 1133 K, (c) 1173 K, (d) 1213 K, and (e) R and $AARE$.

ture of the studied titanium alloy, and the DPT, Ostwald ripening effect, and spheroidization occur simultaneously.

(3) An Arrhenius constitutive equation is established with a correlation coefficient of 0.9848, and the model can be utilized to predict the flow behavior of titanium alloys at high-temperature deformation.

Acknowledgements

This work was financially supported by the Jiangxi Provincial Natural Science Foundation (20232BAB204054, 20242BAB20200, 20252BAC240340), the National Natural Science Foundation (52405356), the Science and Technology Research Project of Jiangxi Provincial Department of

Education (GJJ210670), and the Scientific Research Foundation of East China Jiaotong University.

References

[1] Q. Y Zhao, Q. Y. Sun, S. W. Xin, Y. N Chen, C. Wu, H. Wang, J. W. Xu, M. P. Wan, W. D. Zeng, Y. Q. Zhao, High-strength titanium alloys for aerospace engineering applications: A review on melting-forging process, Materials Science and Engineering: A 845 (2022) 143260. https://doi.org/10.1016/j.msea.2022.143260

[2] J. Cheng, Z. X. Du, X. Y. Zhang, W. Zhang, J. Y. Gai, J. S. Li, Characterization of Ti-25.5 Al-13.5 Nb-2.8 Mo-1.8 Fe alloy hot deformation behavior through processing map, Frontiers in Materials 7 (2020) 23. https://doi.org/10.3389/fmats.2020.00023

[3] L. Li, L. X. Yuan, F. Luo, Y. T. Chen, W. Zhao, X. Q. Li, Microstructure evolution and shear strength of TiAl-based intermetallic joint vacuum brazed with TiH_2-Ni-TiB_2 powder filler, Adv. Eng. Mater. 25 (2023) 2301185. https://doi.org/10.1002/adem.202301185

[4] L. Li, F. Luo, Y. T. Chen, L. X. Yuan, W. Zhao, X. Q. Li, Effect of in-situ synthesized TiB whiskers on interfacial microstructure and shear strength of γ-TiAl joint vacuum brazed with TiH_2-Ni-TiB_2 fillers, Mater. Today. Comm. 38 (2024) 107808. https://doi.org/10.1016/j.mtcomm.2023.107808

[5] G. Liu, Y. G. Su, X. Y. Pi, S.W. Xin, K. Li, D. F. Liu, Y. C. Lin, Achieving high strength 316L stainless steel by laser directed energy deposition-ultrasonic rolling hybrid process, Materials Science and Engineering: A 903 (2024) 146665. https://doi.org/10.1016/j.msea.2024.146665

[5] G. Liu, Y. G. Su, S. W. Xin, C. Y. Li, Z. X. Deng, D. F. Liu, Y. C. Lin, Enhanced wear resistance of Ti reinforced Inconel 718 superalloy manufactured by laser directed energy deposition, Materials Characterization 209 (2024) 113736. https://doi.org/10.1016/j.matchar.2024.113736

[7] C. X. Wang, G. F. Wang, X. Y. Zhang, T. M. Li, J. H. Wang, Q. B. Yang, Microstructural evolution and high-temperature deformation mechanisms in TiB whisker-reinforced near-α titanium matrix composites after superplastic tensile deformation, Journal of Alloys and Compounds, 1044 (2025) 184163. https://doi.org/10.1016/j.jallcom.2025.184163

[8] H. T. Jiao, Y. B. Xu, L. Z. Zhao, R. D. K. Misra, Y. C. Tang, D. J. Liu, Y. Hu, M. J. Zhao, M.X. Shen, Texture evolution in twin-roll strip cast non-oriented electrical steel with strong Cube and Goss texture, Acta Materialia 199 (2020) 311–325. https://doi.org/10.1016/j.actamat.2020.08.048

[9] Z. H. Du, J. Cheng, X. Ran, Z. Wang, Y. X. He, X. H. Zhang, X. Y. Zhu, J. Z. Zhang, W. Xu, X. Lu, Effects of feedstock powder on wear, corrosion, and tribocorrosion performances of Ti-6.5Al-2Zr-1Mo-1V fabricated by additive manufacturing, Journal of Alloys and Compounds 1010 (2025) 177748. https://doi.org/10.1016/j.jallcom.2024.177748

[10] Y. Y. Guo, L. Wu, Y. B. Shang, C. Q. Sun, Effects of defect, mean stress and lower loading on high cycle and very high cycle fatigue behavior of Ti-6Al-4V alloy, Acta Metallurgica Sinica (English Letters) 38 (2025) 435–448. https://doi.org/10.1007/S40195-024-01807-9

[11] F. Liu, X. Y. Shen, Y. Zhang, F. Y. Dong, B. B. Wang, Y. Q. Su, L. S. Luo, J. Cheng, Microstructure and mechanical properties of refractory high-entropy alloys of $NbTaZrMo_x$ system, International Journal of Refractory Metals and Hard Materials 134 (2026) 107457. https://doi.org/10.1016/j.ijrmhm.2025.107457

[12] F. Z. Zhao, R. Zhou, Z. Wang, J. Cai, B. Chen, High temperature fatigue behavior of a near-alpha titanium alloy, International Journal of Fatigue 161 (2022) 106918. https://doi.org/10.1016/j.ijfatigue.2022.106918

[13] F. L. Liu, Y. Chen, C. He, C. Wang, L. Li, Y. J. Liu, Q. Y. Wang, Very long life fatigue failure mechanism of electron beam welded joint for titanium alloy at elevated temperature, International Journal of Fatigue 152 (2021) 06446. https://doi.org/10.1016/j.ijfatigue.2021.106446

[14] G. Li, Y. Y. Guo, S. S. Rui, C. Q. Sun, High-temperature fatigue behavior of TC17 titanium alloy and influence of surface oxidation, International Journal of Fatigue 176 (2023) 107896. https://doi.org/10.1016/j.ijfatigue.2023.107896

[15] M. Kukuryk, Effects of anvils shape and technological conditions on the quality during hot cogging process of the two-phase titanium alloy, International Journal of Material Forming 18 (2025) 83. https://doi.org/10.1007/s12289-025-01944-1

[16] Y. S. Wang, Z. D. Li, H. Y. Wang, M. Y. Hou, K. Yu, Y. P. Xu, H. Xiao, Flow behavior and dynamic recrystallization mechanism of a new near-alpha titanium alloy Ti-0.3Mo-0.8Ni-2Al-1.5Zr, Journal of Materials Research and Technology 30 (2024) 3863–3876. https://doi.org/10.1016/j.jmrt.2024.04.076

[17] X. Zhou, L. Fu, J. Cheng, Y. Mao, Hot deformation characteristics and processing map of Ti-25Al-14Nb-2Mo-1Fe alloy under hot working process conditions, Materials Letters 342 (2023) 134326. https://doi.org/10.1016/j.matlet.2023.134326

[18] J. Cheng, S. Yu, J. S. Li, J. Y. Gai, Z. X. Du, F. Y. Dong, J. Y. Zhang, X. Y. Zhang, Precipitation behavior and microstructural evolution of α phase during hot deformation in a novel β-air-cooled metastable β-type Ti-B12 alloy, Metals 12 (2022) 770. https://doi.org/10.3390/met12050770

[19] G. C. Wu, Y. C. Lin, M. Wan, N. F. Zeng, S. Zhang, H. J. Zhang, M. S. Chen, Y. Q. Jiang, An internal-state-variable-based continuous dynamic recrystallization model for thermally deformed TC18 alloy, Materials 17 (2024) 4026. https://doi.org/10.3390/ma17164026

[20] Y. Q. Jiang, Y. C. Lin, G. Q. Wang, G. D. Pang, M. S. Chen, Z. C. Huang, Microstructure evolution and a unified constitutive model for a Ti-55511 alloy deformed in β region, Journal of Alloys and Compounds 870 (2021) 159534. https://doi.org/10.1016/j.jallcom.2021.159534

[21] X. H. Liu, T. Wang, X. L. Ren, J. Fu, L. Cheng, K. X. Wang, A new microstructural refinement mechanism of ultra-large β grains in near-β titanium alloys during primary hot-working, Materials Letters 346 (2023)134500. https://doi.org/10.1016/j.matlet.2023.134500

[22] Z. K. Yin, Z. C. Sun, J. Cao, L. Huang, Y. Wang, L. J. Yin, Three-dimensional morphology of tri-modal microstructure and evolution mechanisms of constitute phases in dual heat treated near-α titanium alloy, Materials Characterization 185 (2022) 111761. https://doi.org/10.1016/j.matchar.2022.111761

[23] C. Zhang, Y. Gao, X. Y. Liu, Y. X. He, J. Cheng, W. Xu, A comparative study of hot deformation behavior between powder sintering and forged ingot TA15 alloys, Journal of Alloys and Compounds 1031 (2025) 180948. https://doi.org/10.1016/j.jallcom.2025.180948

[24] L. J. Yin, Z. C. Sun, J. X. Fan, Z. K. Yin, Y. Wang, Z. Y. Dang, Dynamic recrystallization in a near β titanium alloy under different deformation modes-transition and correlation, Acta Materialia 276 (2024) 120148. https://doi.org/10.1016/j.actamat.2024.120148

[25] L. Huang, C.M. Li, C. L. Li, S. X. Hui, Y. Yu, M. J. Zhao, S. Q. Guo, J. J. Li, Research progress on microstructure evolution and hot processing maps of high strength β titanium alloys during hot deformation, Transactions of Nonferrous Metals Society of China 32 (2022) 3835–3859. https://doi.org/10.1016/S1003-6326(18)66062-X

[25] S. M. Zhang, W. H. Huang, J. J. Yu, Z. X. Zhang, J. T. Zhang, R. Yuan, C. Zhang, J. Han, J. Meng, T. Wang, Effect of heterogeneous deformation on microstructure and microtexture evolution of Ti-6Al-4V alloy during multidirectional isothermal forging, Advanced Engineering Materials 26 (2024) 2400956. https://doi.org/10.1002/adem.202400956

[27] J. L. Su, X. K. Ji, H. M. Xie, J. Tang, F. L. Jiang, D. F. Fu, J. Teng, H. Zhang, Constitutive and microstructural characteristics of Ti-5Al-2.5Sn alloy during isothermal and non-isothermal multi-stage hot deformation across different phase regions, Journal of Alloys and Compounds 908 (2022) 164647. https://doi.org/10.1016/j.jallcom.2022.164647

[28] X. Q. Jiang, X. G. Fan, M. Zhan, L. Wang, Z. Y. Tan, Y. F. Wang, Y. F. Liang, Lamellar kinking in primary hot working of titanium alloy: Cross-scale behavior and mechanism, Journal of Materials Processing Technology 307 (2022) 117659. https://doi.org/10.1016/j.jmatprotec.2022.117659

[29] Y. C. Lin, X. M. Chen, A critical review of experimental results and constitutive descriptions for metals and alloys in hot working, Materials & Design 32 (2011) 1733–1759. https://doi.org/10.1016/j.matdes.2010.11.048

[30] Y. Y. Man, H. Y. Zhang, J. Cheng, G. Zhou, L. J. Chen, N. N. Zhang, Y. B. Jiang, Y. H. Wang, Phenomenological constitutive model and physical constitutive model of hot deformed dual-phase Ti-5Al-4Sn-2Zr-5Mo alloy, JOM 77 (2025) 1774–1790. https://doi.org/10.1007/s11837-024-06929-0

[31] X. M. Yang, J. H. Zhao, X. W. Yan, X. N. Shi, H. Z. Guo, The dynamic softening identification and constitutive equation establishment of Ti-6.5Al-2Sn-4Zr-4Mo-1W-0.2Si alloy with initial lamellar microstructure, High Temperature Materials and Processes 41 (2022) 669–682. https://doi.org/10.1515/htmp-2022-0242

[32] H. M. Zhang, X. Y. Mao, S. Xu, N. M. Xiao, N. Zhang, Z. S. Cui, A physically based elasto-viscoplastic constitutive model for modeling the hot deformation and microstructure evolution of a near α Ti alloy, Materials Science and Engineering: A 872 (2023) 144994. https://doi.org/10.1016/j.msea.2023.144994

[33] R. H. Buzolin, M. Lasnik, A. Krumphals, M. C. Poletti, A dislocation-based model for the microstructure evolution and the flow stress of a Ti5553 alloy, International Journal of Plasticity 136 (2021) 102862. https://doi.org/10.1016/j.ijplas.2020.102862

[34] J. S. Jha, S. P. Toppo, R. Singh, A. Tewari, S. K. Mishra, Flow stress constitutive relationship between lamellar and equiaxed microstructure during hot deformation of Ti-6Al-4V, Journal of Materials Processing Technology 270 (2019) 216–227. https://doi.org/10.1016/j.jmatprotec.2019.02.030

[35] G. C. Wu, Y. C. Lin, M. S. Chen, W. Qiu, N. F. Zeng, S. Zhang, M. Wan, D. G. He, Y. Q. Jiang, M. Naseri, Continuous dynamic recrystallization behaviors in a single-phase deformed Ti-55511 alloy by cellular automata model, Journal of Alloys and Compounds 1002 (2024) 175293. https://doi.org/10.1016/j.jallcom.2024.175293

[36] M. Wan, Y. C. Lin, N. F. Zeng, M. S. Chen, C. Li, X. D. Zhan, G. C. Wu, S. Zhang, Perception and reconstruction of temperature field in forgings based on physical model and CNN model, Measurement 242 (2025) 116210. https://doi.org/10.1016/j.measurement.2024.116210

[37] A. E. Marques, T. G. Parreira, A. F. G. Pereira, B. M. Ribeiro, P. A. Prates, Machine learning applications in sheet metal constitutive modelling: A review, International Journal of Solids and Structures 303 (2024) 113024. https://doi.org/10.1016/j.ijsolstr.2024.113024

[38] V. V. Pogorelko, A. E. Mayer, E. V. Fomin, E. V. Fedorov, Examination of machine learning method for identification of material model parameters, International Journal of Mechanical Sciences 265 (2024) 108912. https://doi.org/10.1016/j.ijmecsci.2023.108912

[39] T. W. Wu, Z. P. Gao, M. H. Chen, H. R. Dong, Data-driven time series analysis for high-temperature deformation behavior prediction based on the deep learning approach: A case study on titanium alloy, Journal of Alloys and Compounds 1037 (2025) 182233. https://doi.org/10.1016/j.jallcom.2025.182233

[40] Z. Q. Hong, Y. Niu, Y. Q. Wang, Y. C. Zhu, Prediction of flow stress in isothermal compression of hydrogenated TC17 alloy using multiple prediction models, Materials Today Communications 38 (2024) 108011. https://doi.org/10.1016/j.mtcomm.2023.108011

[41] Y. Kim, H. Y. Jeong, J. Park, K. Kim, H. Kwon, G. Ju, N. Kim, Optimizing process parameters for hot forging of Ti-6242 alloy: A machine learning and FEM simulation approach, Journal of Materials Research and Technology 27 (2023) 8228–8243. https://doi.org/10.1016/j.jmrt.2023.11.193

[42] Y. S. Wang, G. Yang, S. N. Zhang, S. C. Xiu, Effect of crystal orientation on micro-stress distribution in a damage-tolerant titanium alloy TC21, Journal of Alloys and Compounds 924 (2022) 166637. https://doi.org/10.1016/j.jallcom.2022.166637

[43] X. Li, D. L. Ouyang, K. M. Zhang, K. L. Wang, X. Cui, Hot deformation characteristic of TC21 titanium alloy with lamellar microstructure, Materials Today Communications, 39 (2024) 108709. https://doi.org/10.1016/j.mtcomm.2024.108709
[44] X. Li, C. W. Huang, J. Yang, F. Liu, S. Y. Wei, M. P. Wan, F. Zhao, Y. Q. Zhao, Optimization of quasi-β forging parameters to control trimodal microstructure parameters and performance of TC21 forgings, Materials Science and Engineering: A 909 (2024) 146824. https://doi.org/10.1016/j.msea.2024.146824
[45] X. Wen, M. P. Wan, C. W. Huang, Y. B. Tan, M. Lei, Y. L. Liang, X. Cai, Effect of microstructure on tensile properties, impact toughness and fracture toughness of TC21 alloy, Materials & Design 180 (2019) 107898. https://doi.org/10.1016/j.matdes.2019.107898
[46] Y. Q. Jiang, Y. W. Guo, M. B. Wang, J. J. Han, Z. C. Huang, Z. F. Huang, Hot deformation and constitutive modeling of a Ti-Al-Sn-Zr-Mo-Cr-Nb alloy, Materials Today Communications 40 (2024) 110037. https://doi.org/10.1016/j.mtcomm.2024.110037
[47] Y. Q. Jiang, M. B. Wang, Y. F. Zhang, J. J. Han, Z. H. Li, Y. Y. He, D. Wu, Z. F. Huang, Process-dependent microstructural evolution of a hot-deformed damage tolerance titanium alloy, Journal of Materials Research and Technology 39 (2025) 4512–4521. https://doi.org/10.1016/j.jmrt.2025.10.142
[48] Y. Dong, X. G. Liu, H. Xu, Y. N. He, Y. J. Ke, W. W. Zhang, Relationship between $\beta \rightarrow \alpha$ dynamic transformation and dynamic recrystallization under thermo-mechanical coupling in Ti-5Al-5Mo-5V-1Cr-1Fe alloy, Journal of Materials Science & Technology 179 (2024) 98–113. https://doi.org/10.1016/j.jmst.2023.05.061
[49] J. Wang, X. H. Ji, B. Ouyang, X. S. Chang, Y. S. Qi, G. Chen, Y. B. Li, Post-dynamic transformation from α to β phase and reverse transformation in Ti-10V-2Fe-3Al alloy during interrupted hot deformation, Journal of Alloys and Compounds 997 (2024) 174884. https://doi.org/10.1016/j.jallcom.2024.174884
[50] X. G. Liu, H. Z. Niu, S. Z. Zhao, Y. X. Feng, Y. Dong, J. Liu, P. W. Liu, Microstructural evolution and prediction of TC18 titanium alloys by high-throughput technology and machine learning, Journal of Alloys and Compounds 1017 (2025) 179202. https://doi.org/10.1016/j.jallcom.2025.179202
[51] E. Zhu, F. G. Li, Q. Zhao, X. H. An, S. Farah, K. N. Yao, Phase transformation and deformation behavior under isothermal compression in β-quenched metastable Ti-10V-2Fe-3Al alloy, Materials Today Communications 38 (2024) 107727. https://doi.org/10.1016/j.mtcomm.2023.107727
[52] C. Liu, F. Y. Dong, Y. Zhang, X. G. Yuan, B. B. Wang, L. S. Luo, Y. Q. Su, J. Cheng, P. K. Liaw, Morphology, microstructure, and mechanical properties of TiZrTa0.7NbMo refractory high-entropy alloy spherical powder prepared by ultrasonic atomization, Intermetallics 187 (2025) 109019. https://doi.org/10.1016/j.intermet.2025.109019
[53] S. X. Shi, J. Y. Ge, X. Y. Zhang, Q. X. Liu, R. S. Li, BPANN modified constitutive descriptions for flow behavior and softening mechanism in the $\alpha + \beta$ phase region of Ti-55511 alloy with equiaxed microstructure, Journal of Materials Research and Technology 28 (2024) 3722–3734. https://doi.org/10.1016/j.jmrt.2023.12.194
[54] X. Ma, W. D. Zeng, F. Tian, Y. G. Zhou, Y. Sun, Optimization of hot process parameters of Ti-6.7Al-2Sn-2.2Zr-2.1Mo-1W-0.2Si alloy with lamellar starting microstructure based on the processing map, Materials Science and Engineering: A 545 (2012) 132–138. https://doi.org/10.1016/j.msea.2012.03.011